Water Resources Research

RESEARCH ARTICLE
10.1029/2019WR024992

Water Vapor Sorption Properties of Illinois Shales Under Dynamic Water Vapor Conditions: Experimentation and Modeling

Guijie Sang[1], Shimin Liu[1], and Derek Elsworth[1]

[1]Department of Energy and Mineral Engineering, G3 Center and EMS Energy Institute, The Pennsylvania State University, University Park, PA, USA

Key Points:
- Mesopore condensation dominates at high humidity for shales without expansive clays while is nondominant for shale with montmorillonite
- Montmorillonite contains large interlayer spaces, which is accessible to water molecules but inaccessible to N_2 molecules
- Kerogen containing high oxygen-containing functional groups may lead to high water adsorption for organic-rich shales

Supporting Information:
- Supporting Information S1

Correspondence to:
S. Liu,
szl3@psu.edu

Citation:
Sang, G., Liu, S., & Elsworth, D. (2019). Water vapor sorption properties of Illinois shales under dynamic water vapor conditions: Experimentation and modeling. *Water Resources Research*, *55*, 7212–7228. https://doi.org/10.1029/2019WR024992

Received 13 FEB 2019
Accepted 6 AUG 2019
Accepted article online 10 AUG 2019
Published online 23 AUG 2019

Abstract Water vapor adsorption/desorption isotherms are measured on five shales from Illinois basin by dynamic vapor sorption method. The experimental adsorption data are modeled by the Guggenheim, Anderson, and De Boer model and the Freundlich model over the entire range of measured relative humidity (R_h) values (0–0.95). Modeling results show that shale hydration is controlled by surface chemistry at low R_h through a strong intermolecular bonding, while is mainly influenced by the pore structure at high R_h (>0.9) through capillary condensation. This is consistent with the progressive decrease of isosteric heat of adsorption with water content, obtained by the Clausius-Clapeyron equation. Exceptionally, for the one shale containing 8.6% montmorillonite, mesopore condensation only accounts for 33% of the measured water adsorption even at R_h ~0.95 due to the limited external pores and the important role of clay swelling. The specific surface area defined by Guggenheim, Anderson, and De Boer analysis as available for water adsorption is larger than that available for low-pressure N_2 adsorption due to the complex surface chemistry. The one shale rich in expansive montmorillonite and with a large interlayer capacity for water but inaccessible to N_2 molecules conditions this result. Among the other four shales, one with high kerogen content behaves the highest water adsorption, possibly due to the high content of oxygen-containing functional groups and the potentially high pore volume of kerogen. These findings contribute to a better understanding of water storage and transport behavior in shales and impact behavior relevant to structures and reservoirs founded in such media.

1. Introduction

The petrophysical and petrochemical properties of shales have been extensively investigated in the geosciences, materials-, and engineering-sciences related to hydrocarbon extraction (Curtis, 2002) and environmental protection (Jackson et al., 2013; Vidic et al., 2013), injection-induced seismicity (Elsworth et al., 2016), wellbore stability (Chen et al., 2003), ground control issues in underground coal mines (Chugh & Missavage, 1981; Van Eeckhout, 1976), geological disposal of radioactive wastes (Gautschi, 2001), and CO_2 sequestration in depleted shale reservoirs (Busch et al., 2008; Guiltinan et al., 2017). An important component in many of these studies is in understanding mechanisms of shale-water interaction due to liquid and water vapor uptake as driven by different processes. Although a broad spectrum of possible mechanisms have been reported for shale hydration, including capillary suction, osmotic attraction, and the role of other surfaces forces such as hydrogen bonding, cation hydration, Van de Waal, and other forces (Derjaguin, 1992; Li et al., 2016; Tuller et al., 1999), water sorption behavior on shale and the role of pore structure and complex mineralogy on hydration mechanisms remain incompletely understood. A microscale study of water vapor sorption on shales will illuminate potential shale hydration mechanisms to enhance fundamental understanding of water-shale interactions.

Water vapor adsorption on shales and other mudrocks has been studied to investigate the relationship between pore structure and hydration behavior. Based on the presumption that water molecules will not condense within hydrophobic organic pores, water sorption isotherms (Zolfaghari, Dehghanpour, & Holyk, 2017; Zolfaghari, Dehghanpour, & Xu, 2017) may be used as a proxy to characterize pore size distribution. The utilization of this proxy is robust, unless surface chemistry rather than pore structure controls water adsorption at low relative humidity (R_h) (Seemann et al., 2017; Thommes et al., 2013). Additionally, water molecules may also adsorb to the organic matter on the interior pore surfaces by hydrogen bonding

with oxygen-containing functional groups and/or condense in these organic pores (Allardice & Evans, 1971; Nishino, 2001). Water sorption isotherm data on thirteen mudrocks (Seemann et al., 2017) have been fit to varied physisorption models including BET (Brunauer et al., 1938), BJH (Barrett et al., 1951), and Dubinin (Dubinin, 1960) models with the various authors concluding that direct relationships between water adsorption and pore structure do not exist since pore surface chemistry dominates the water adsorption response at low relative humidities. However, the pore structure based on low-pressure nitrogen adsorption technique may not precisely represent the pore structure of shale containing expansive clays such as montmorillonite, which may contain large amount of "internal" pore spaces inaccessible to nitrogen molecules (Aylmore & Quirk, 1967; Diamond & Kinter, 1956; Hendricks et al., 1940; Mooney et al., 1952a). Thus, multiple pore characterization and imaging techniques (Clarkson et al., 2013; Macht et al., 2011) may be required for a better understanding of the correlation between water vapor adsorption and pore structure. The water adsorption behavior on Marcellus shale has been characterized by thermal gravimetric sorption (TGA-SA) at various temperatures (Tang et al., 2017). The Dent multilayer adsorption model was found to reasonably represent the water vapor adsorption isotherms and estimate adsorption on both primary and secondary sorption sites. However, hydration mechanisms in the clay-water and kerogen-water systems that involve physicochemical interactions are expected to differ from those of pure physical sorption—such underlying mechanisms are difficult to deconvolve since shales are typically complex and heterogeneous and contain mixtures of minerals and kerogen types.

Hydration mechanisms in shales depend on mineralogy and physicochemical structure and are considerably more complex than that in coals or conventional reservoir rocks. This added complexity results from the presence of both strongly hydrophilic clay minerals and overall hydrophobic/hydrophilic organic kerogen. The hydrophobicity/hydrophilicity of the organic kerogen depends strongly on its thermal maturity and the composition of its functional groups (Hu et al., 2014, 2016). Kaolinite, illite, and montmorillonite, which may be present in varying proportions in typical shales, have different water vapor adsorption capacities and swelling properties depending on their crystalline structure, cation exchange capacity (CEC), specific surface area (SSA), and particle size. Nonexpansive 1:1-type kaolinite and 2:1-type illite have less overall water adsorption capacity due to smaller SSA and CEC. In comparison, 2:1-type montmorillonite with a higher SSA and CEC exhibits greater potential for adsorption and swelling due to interlayer cation hydration (Sposito, 2008; Woodruff & Revil, 2011). Unlike purely hydrophilic minerals that dominate conventional reservoir rocks, pores in kerogen may have mixed-wetting characteristics (i.e., simultaneous hydrocarbon-wetting and water-wetting) depending on maturity level (Hu et al., 2014, 2016). Lower maturity kerogens generally have both higher oxygen to carbon ratios and denser oxygen-containing functional groups—these are intrinsically more hydrophilic-prone than more mature and overmatured kerogens. Similar phenomena have also been reported for coal—recovered from measurements of water-coal contact angles—revealing that coal contains a full spectrum of strongly hydrophobic sites, weakly hydrophobic sites, and hydrophilic sites (Gutierrez-Rodriguez et al., 1984). Since kerogen shares similar functional groups with coal (high kerogen content), kerogen may also play a similarly important role in water vapor adsorption on organic-rich shales.

To date, the underlying hydration mechanisms in shales with complex mineral compositions and pore structures are still not fully understood. The role of minerals on the water hydration has been investigated, but the influence of nanopore structure on water storage capacity has not been comprehensively studied. The novelty of this study is to interrelate the pore structure and the mineral composition to the water vapor sorption behavior on nanoporous shales and thus to provide an improved understanding of hydration mechanisms in different mineralogical compositions including nonexpansive clays, expansive montmorillonite, and kerogen. The study measures water vapor adsorption/desorption isotherms for five different shale samples (three gray shales and two black shales) from the Illinois basin by dynamic vapor sorption (DVS). The adsorption isotherms are analyzed and fitted to a Guggenheim, Anderson, and De Boer (GAB) model and to a Freundlich model over the applicable range of R_h values. Shale hydration mechanism at different R_h values are discussed using combined GAB and Freundlich analyses inclusive of isosteric heat of sorption, which is calculated based on the well-known Clausius-Clapeyron equation. Additionally, SSAs measured by water and N_2 adsorption are contrasted, and the correlation between water adsorption and N_2 adsorption is discussed. Furthermore, role of mesopore condensation in water adsorption at different R_h values is also quantitatively studied based on the characterized pore size distribution and the well-known Kelvin equation. Finally, the relative roles of clays and kerogen in shale hydration are discussed.

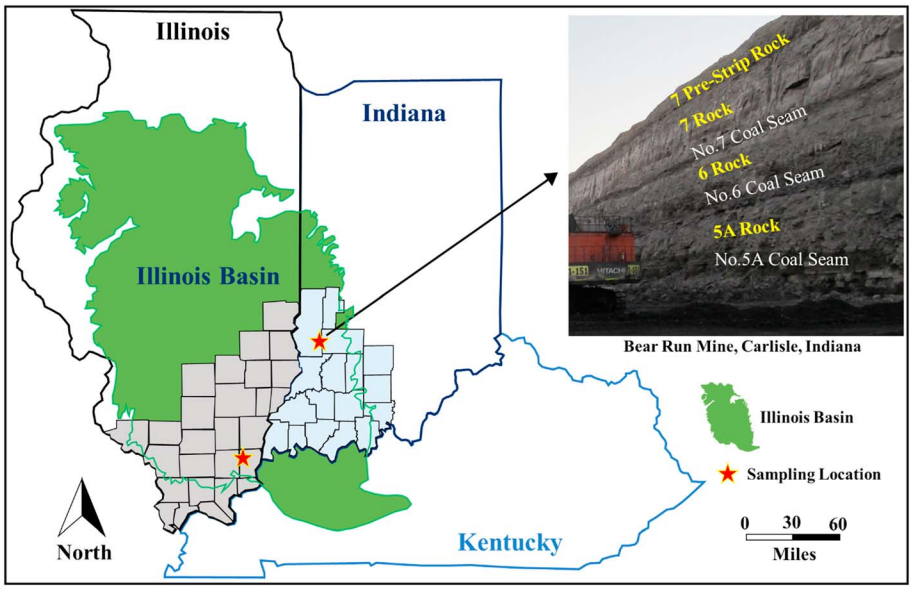

Figure 1. Shale sampling locations from coal mines in the Illinois basin.

2. Materials and Methods

2.1. Sample Collection, Preparation, and Characterization

A total of five different shale samples were collected from two coal mines in Illinois basin (Figure 1). Among the five shale samples, four (6R, 6F, 5A, and 7R) were collected from the Bear Run Mine located at Carlisle, Indiana, with the final sample (H6) recovered from the Wildcat Hills Mine located at Equality, Illinois. The samples are labeled relative to the adjacent coal seams. The lithostratigraphic column of the sampled strata is illustrated in Figure 1 with the four shale samples 6R, 6F, 5A, and 7R named after their corresponding coal seams (i.e., 6R gray shale and 6F black shale from No. 6 coal seam [Hymera], 5A gray shale from No. 5A coal seam [Springfield], and 7R gray shale from No. 7 coal seam [Danville], and H6 for the Herrin No. 6 coal seam). Among the five shale samples, the three gray shales (6R, 5A, and 7R) have no organic content (TOC ~0%) with the two black shales containing ~31.4% (6F) and ~21.4% (H6) TOC. The thermal maturity of the organic shales (6F and H6) is indexed by vitrinite reflectance (R_o) of the kerogen—as 0.31% (6F) and 0.71% (H6), indicating a fairly low maturation. The mineralogical compositions for each sample are listed in Table 1. The three gray shales (6R, 5A, and 7R) share the same type of mineral compositions with no pyrite and carbonates, while the two black shales contain similar amounts of pyrite (2.7% and 3.1%, respectively) with the 6F shale containing 1.4% calcite and the H6 shale containing 3.3% dolomite. Overall the five shale samples have relatively high illite contents, among which black shale H6 contains both the highest illite (29.3%) and montmorillonite (8.6%) contents. The functionalized oxygen-to-carbon (O/C) atomic ratio are 20.4% (±0.6%) for 6F shale and 5.0% (±1.6%) for H6 shale, which were measured by X-Ray Photoelectron Spectroscopy in Materials Characterization Laboratory at Penn State University.

2.2. Pore Structure Characterization

Low-pressure N_2 adsorption at 77 K were performed on all five shale powder samples (60–80 mesh) using a Micromeritics ASAP 2020 in the Materials Characterization Laboratory at Penn State University. Prior to each N_2 adsorption experiment, the shale sample was automatically degassed at ~80 °C for ~16 hr to avoid potential damage of kerogen in the two black shales. Compared to the low pressure N_2 adsorption experiment for pore characterization, mercury intrusion porosimetry (MIP) for one gray shale (5A) and the two black shales (6F and H6) were also performed using a Micrometrics Autopores V 9620 located in the Materials Characterization Laboratory at Penn State University. A detailed description of the N_2 adsorption results (6R, 5A, 6F, and H6) and MIP results (5A, 6F, and H6) have been reported in a previous study (Sang et al., 2018).

Table 1
Mineralogical Composition of Shale Samples Based on XRD Analysis (%)

		Clays		Mica	Other phyllosilicate minerals					Feldspar		Carbonates		TOC[b,c]
Sample	Quartz	Illite	Mont.[a]	Muscovite	Chlorite	Clinochlore	Dickite	Halloysite	Palygorskite	Albite	Pyrite	Calcite	Dolomite	TOC
6R	14.2	21.5	—	29.3	—	28.9	3.4	—	—	2.7	—	—	—	—
5A	17.3	27.7	—	21.2	—	14.7	15.7	—	—	3.4	—	—	—	—
7R	26.6	29.9	—	12.3	—	11.7	9.7	—	—	9.9	—	—	—	—
6F	16.7	20.1	—	6.0	8.6	—	—	—	12.3	0.8	2.7	1.4	—	31.4
H6	17.7	29.3	8.6	5.0	—	—	—	11.6	—	—	3.1	—	3.3	21.4

Note. XRD = X-ray diffraction.
[a]Mont. stands for montmorillonite. [b]TOC refers to total organic carbon (kerogen). The vitrinite reflectance (R_o) of kerogen in 6F and H6 were 0.31% and 0.71%, respectively. [c]The functionalized oxygen-to-carbon (O/C) atomic ratio are 20.4% (±0.6%) for 6F shale and 5.0% (±1.6%) for H6 shale, which were measured by X-Ray Photoelectron Spectroscopy in Materials Characterization Laboratory at Penn State University.

2.3. DVS

Water vapor sorption isotherms were recovered for powdered samples of the shale using DVS. The DVS instrument (Figure 2) accurately determines water vapor ad/desorption isotherms as well as kinetics at each pressure step. During each experiment, a gas flow stream with a fixed flow rate of 200 standard cubic centimeters per minute (sccm) was continuously supplied into the sample chamber. The relative humidity, equivalent to the partial pressure ratio p/p_0 of water vapor, was adjusted by two mass flow controllers by mixing a dry N_2 stream with a wetting N_2 stream containing 100% humidity. The mass change of the sample due to water vapor ad/desorption was continuously monitored and recorded by an ultrasensitive microbalance capable of measuring to a resolution of 0.1 μg ± 1%. To avoid potential condensation of vapor in the balance chamber and to ensure optimal performance of the microbalance, dry purge gas was constantly flowed through the balance chamber at a rate of 70 ± 10 sccm and a temperature of 40 °C. Powdered samples (60–80 mesh) in native state in batches of ~10–20 mg were loaded onto a small pan suspended on a microbalance. The R_h value started from 0 to achieve the initial dry condition, followed by a full cycle of adsorption/desorption measurement with a stepwise increase/decrease of R_h by ±0.1. The equilibrium state is defined when mass change is less than or equal to 0.002% per minute and maintained stable for ten minutes. For each sample, three temperatures (20, 30, and 40 °C) were performed to obtain each ad/desorption isotherm. The reproducibility of the laboratory results was confirmed by performing three repeats of each experiment.

Figure 3 shows a typical suite of raw data for water vapor sorption on the black shales (6R and H6) for a full wetting and drying cycle at 30 °C. Under initial dry conditions (R_h~0%), the residual water desorbs and mass of the sample decreases to a constant value—taken as the mass of the dry sample (or reference mass). Water vapor adsorption/desorption isotherms are then directly recovered from the difference between the reference mass and the equilibrium mass of shale samples at a prescribed R_h.

3. Results and Discussion

GAB and Freundlich models, together with an analysis of the isosteric heat of sorption, are applied to study the water vapor sorption behavior of the five shale samples. Please refer to the appendix for the details of these models and theories. In particular, we focus on determining SSA using two probing gases (N_2 and H_2O) and use these outcomes to describe respective sorption mechanisms. These contrasting behaviors are then linked to the roles of clay minerals and kerogen in controlling shale hydration processes as a function of R_h.

3.1. Water Sorption Isotherms

The water vapor ad/desorption isotherms for all five shale samples at 30 °C are presented in Figure 4. These adsorption isotherms follow type Π adsorption patterns according to International Union of Pure and Applied Chemists classification (Thommes et al., 2015) except for the H6 black shale. As is shown in Figure 4, the adsorption isotherm of the H6 shale is similar to type Π except at high R_h (>0.85) where it shows no obvious condensation. The water adsorption isotherms (Figure 4) are sample dependent,

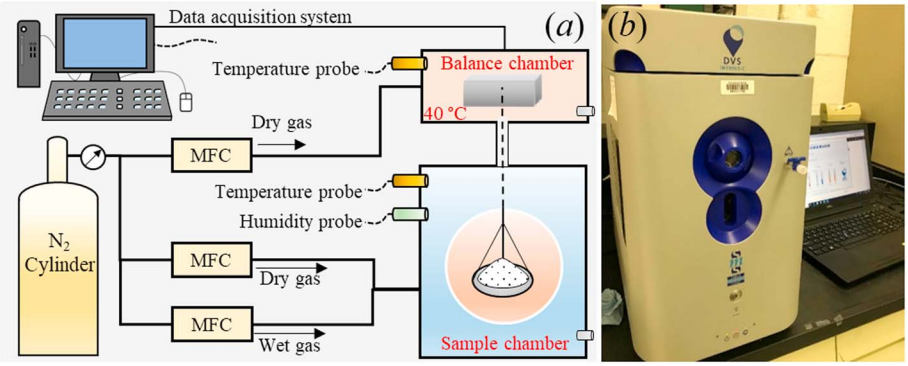

Figure 2. Dynamic vapor sorption (DVS) apparatus. (a) Schematic and (b) photograph. MFC refers to the mass flow controller.

resulting from the specific variations of mineralogical composition and/or pore morphology. Unlike N_2 sorption, which is predominantly controlled by pore structure, water vapor sorption behavior in shales is known to be influenced by the combined effects of surface chemistry and micropore structure (Seemann et al., 2017; Thommes et al., 2013). Based on the X-ray diffraction results, samples 6R, 5A, 7R, and 6F contain no expansive clay minerals. The water adsorption rates of these four shales vary with R_h from the range 0 to ~0.95. These type Π adsorption isotherms can be divided into three segments, as shown in Figure 4: (a) a rapid increase in sorption mass/volume at low R_h (0–0.25) where monolayer adsorption dominates, (b) a moderate increase over the intermediate R_h range (0.25–0.85) where multilayer sorption occurs after monolayer adsorption is complete, and finally, (c) a rapid increase in sorption at high R_h (0.85–0.95) that continues, without reaching a plateau, where capillary condensation dominates (Allardice & Evans, 1971; Tang et al., 2017; Wan et al., 2016). However, for the H6 black shale, containing 8.6% montmorillonite, only one inflection point is observed (R_h ~0.25), dividing the adsorption isotherm into only two segments—a rapid increase at low R_h (<0.25) followed by a linear low-gradient segment between $0.25 < R_h < 0.95$. This is consistent with water adsorption isotherms for montmorillonite reported in the literature (Hatch et al., 2012) with linear form at high R_h. Thus, multilayer adsorption, followed by capillary condensation, may not be an appropriate mechanism for the hydration of shales containing montmorillonite (Feng et al., 2018; Hatch et al., 2012), which rather shows a stepwise interlayer hydration mechanism and exhibits sigmoid-type adsorption curves (Cases et al., 1997; Ferrage et al., 2010; Mooney et al., 1952b). This has also been validated by X-ray diffraction profiles recovered for montmorillonite under controlled humidity (Bérend et al., 1995; Cases et al., 1997; Ferrage et al., 2010). Instead of the sigmoid-type adsorption curves, representing the transitions from zero to one to two interlayer water sheets, the adsorption isotherm of the H6 shale is smooth and unstepped. This can be attributed to a collective effect of capillary condensation in the shale micropores/mesopores at high R_h

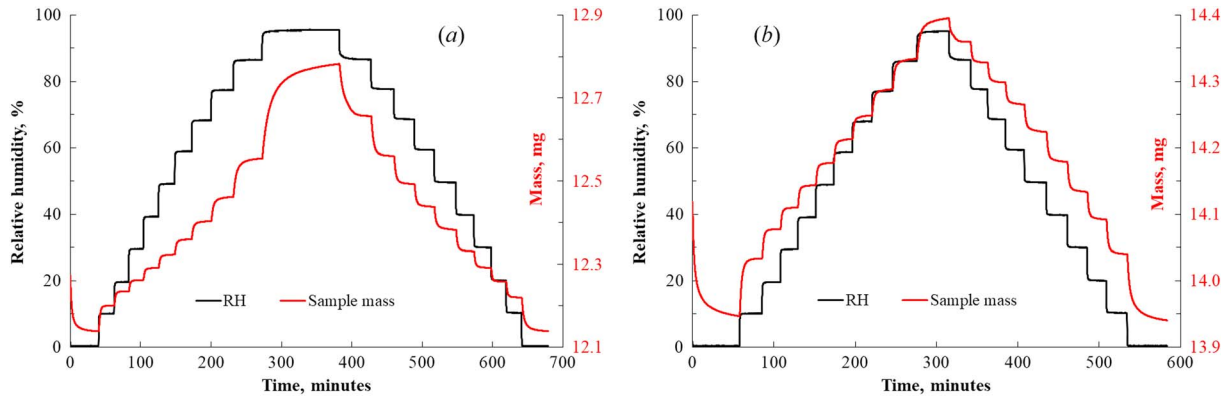

Figure 3. Typical water vapor sorption measurements—raw data recovered from the dynamic vapor sorption analyzer for the black shales: (a) Sample 6F and (b) Sample H6, both at 30 °C.

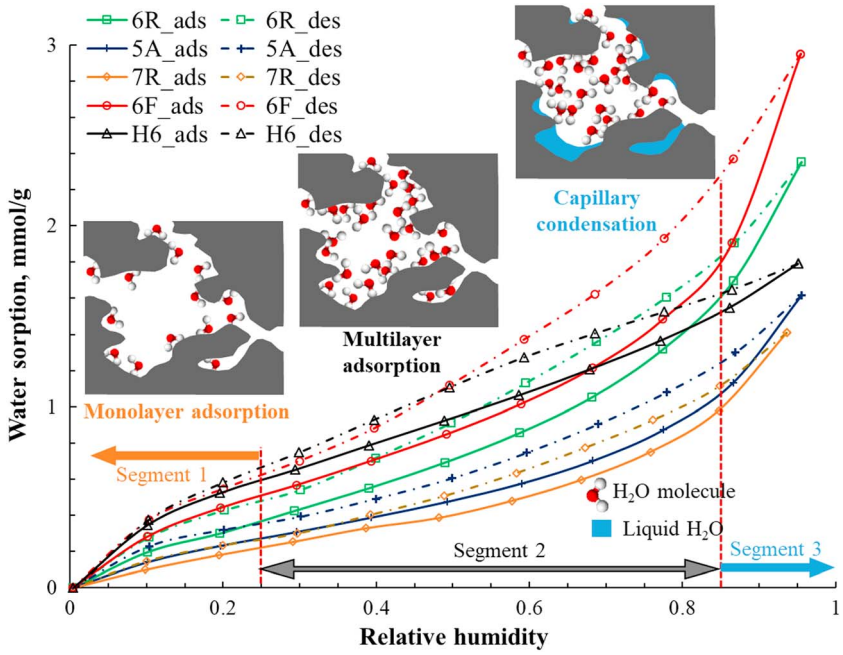

Figure 4. Water vapor ad/desorption isotherms for the five shale samples at 30 °C.

and hydration heterogeneity (Cases et al., 1997; Ferrage et al., 2005, 2010; Michot et al., 2005), which is caused by a continuous distribution of hydration states in montmorillonite.

Among samples 6R, 5A, 7R, and 6F (Figure 4), the 6F black shale has the highest water vapor adsorption while the 7R gray shale has the lowest over the entire range of R_h. This finding is consistent with the N_2 adsorption results (Figure 5) and MIP results (Figure 6), demonstrating that relatively high total pore volume and/or SSA tend to have a higher water adsorption capacity for shales containing negligible fractions of expansive clays. The discrepancy in the mass/volume of water versus N_2 adsorption at the same relative pressure is mainly attributed to, apart from pore-water interaction, the involvement of surface chemistry controlled by mineral surfaces, cation types, functional groups and wettability (Akin & Likos, 2014; Hu et al., 2014; Thommes et al., 2013). Comparing Figure 4 to Figures 5b and 6b, despite representing the lowest pore volume and/or SSA recovered from N_2 adsorption and MIP results, the H6 black shale shows the highest water adsorption at low R_h (<0.6) and an intermediate value at high R_h (>0.85). The intelayer cation hydration of expansive montmorillonite may be the root cause of the remarkable water adsorption capacity of the H6 shale at $R_h < 0.6$. Apparently, the interlayer surface area of montmorillonite, which is far larger than its external surface area, is inaccessible to N_2 moleclues and this may preclude its probing by low-pressure N_2 adsorption technique (Aylmore & Quirk, 1967; Diamond & Kinter, 1956; Hendricks et al., 1940; Mooney et al., 1952a) and MIP technique (Sang et al., 2018). Apparent from the N_2 adsorption results and MIP results (Figures 5b and 6b, respectively), the external pore volume and SSA for the black shale (H6) are a minimum which explains the low water vapor adsorption capacity for $R_h > 0.85$—where water consendation may be limited by small external pore spaces. This is also apparent in the trend of adsorption isotherm that H6 exhibits a less sharp water uptake at $R_h > 0.85$ than other shales. The lack of an obvious upwards concave portion of the isotherm for H6 shale at high R_h may be attributed to the reduced dominance of vapor condensation due to the limited "external" pore volume. It is notable that capillary condensation in shale micropores/mesopores, together with hydration heterogeneity in montmorillonite (Cases et al., 1997; Ferrage et al., 2005, 2010; Michot et al., 2005), results in the smoothing of the hydration isotherm in the H6 shale at high R_h (>0.85).

3.2. Hysteresis Behavior of Tested Shales

The hysteresis of water vapor ad/desorption on shale has been reported in previous studies (Seemann et al., 2017; Tang et al., 2017; Zolfaghari, Dehghanpour, & Holyk, 2017). The water vapor ad/desorption isotherms

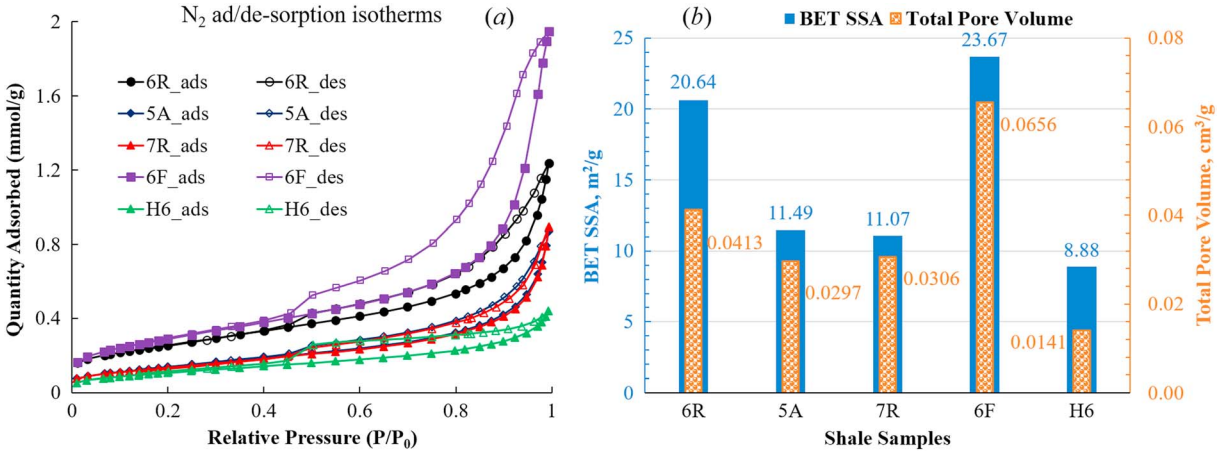

Figure 5. Low-pressure N_2 sorption results: (a) N_2 adsorption/desorption isotherms; (b) BET SSA and total pore volume. SSA = specific surface area.

of the five shale samples are hysteretic, which may be explained by the following mechanisms. At high R_h values where there exists capillary menisci or water film, the hysteresis is usually associated with differences in mechanisms of condensation and evaporation due to the structural heterogeneity of the mesopores. This includes the role of specific curvature in contact with the vapor at a specified relative pressure during capillary condensation being different from that during evaporation (Gregg et al., 1967; Katz, 1949; Sing, 1985). At low R_h values where sorption-water dominates, the sorption hysteresis can be related to particle surface hydration controlled by the adsorptive surface forces (Lu & Khorshidi, 2015; Tuller et al., 1999). For H6 shale containing expansive montmorillonite, the hysteresis of water vapor sorption at low R_h values could also be involved with the crystalline cation hydration in montmorillonite, since the intermolecular forces between crystalline layers during cation hydration is stronger than that during dehydration due to clay swelling, causing cation hydration harder to occur than dehydration (Lu & Khorshidi, 2015).

3.3. Modeling Analyses

3.3.1. GAB Modeling Analysis

The measured water vapor sorption isotherms were fitted and analyzed by the GAB model (see the details in the Appendix A1) over the entire R_h range (0–0.95). Table 2 presents the GAB parameters including V_m, C, and a correction factor K. The corresponding goodness of fit indexes of the GAB model are also shown in Table 2, indicating the remarkable fit of the results ($R^2 > 0.99$). Apart from the GAB model, BET multilayer sorption theory may also work for the interpretation of water vapor sorption data at lower R_h ranges (0.05–0.35) (Do, 1998). However, for the five clay-rich shales especially H6 shale, which contains a fairly amount of expansive montmorillonite, BET model may fail to interpret monolayer coverage of water vapor due to the

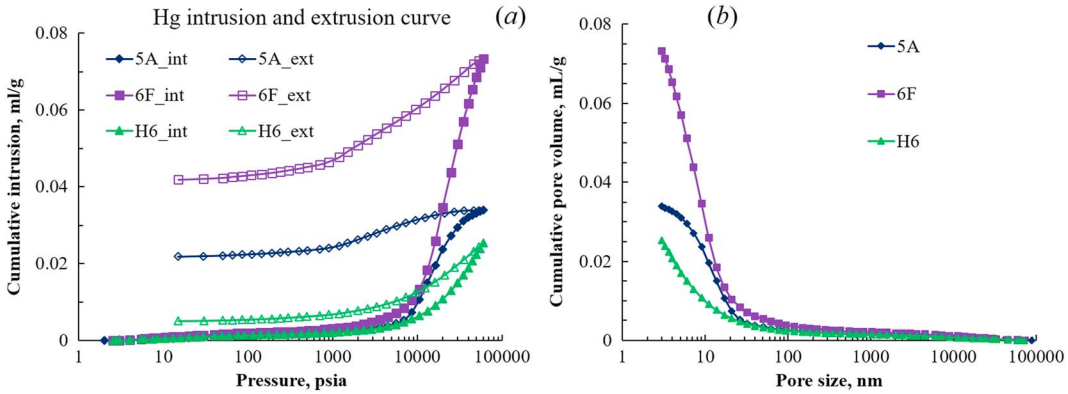

Figure 6. Mercury intrusion porosimetry results for 5A, 6F, and H6 shale: (a) Mercury in/extrusion curves (Sang et al., 2018); (b) cumulative pore volume.

Table 2
GAB Modeling Parameters of Adsorption Isotherms (0–0.95) for the Five Shales at 30 °C

Model type	Shale type	Model coefficients				Goodness of fit indexes		
		V_m	C	K	RH_c	SSE	R^2	RMSE
GAB (0–0.95)	6R	0.53	5.09	0.82	0.37	8.47E−04	0.999	1.03E−2
	5A	0.33	7.46	0.84	0.32	3.84E−04	0.999	0.69E−2
	7R	0.29	5.74	0.86	0.34	3.92E−04	0.999	0.70E−2
	6F	0.51	13.17	0.87	0.25	1.51E−02	0.998	4.34E−2
	H6	0.80	9.84	0.61	0.39	8.59E−04	0.999	1.04E−2

Note. RH_c refers to the critical R_h at which monolayer coverage completes for GAB fit. RMSE = root-mean-square error; SSE = sum of squares of the error.

involvement of cation hydration and/or induced clay swelling (Akin & Likos, 2014; Khorshidi et al., 2017). Instead, the GAB model is recommended for the estimation of monolayer sorption and surface area and (Arthur et al., 2018; Timmermann, 2003). As a matter of fact, GAB equation reduces to the BET equation if $K = 1$, under which circumstances the heat of multilayer adsorption is equal to the heat of liquefaction. K values in Table 2 are less than 1, indicating that heat of multilayer adsorption of water molecules is less than the heat of liquefaction (Arthur et al., 2016, 2018). Therefore, in this study, we apply GAB parameters to describe respective sorption mechanisms in the five shales.

From Table 2, the two black shales (6F and H6) behave higher C values, indicating stronger binding strength of water to the primary binding sites than the three gray shales. Highest C value for the 6F black shale may be due to the high content of the hydrophilic oxygen-containing functional groups (O/C = 20.4%) in the immature organic matter (R_o = 0.31%), providing principal sites for strong hydrogen bonding (Allardice & Evans, 1971; Nishino, 2001). The relatively high C value for the H6 black shale possibly results from the strong intermolecular bonding between water molecules and shale surfaces, including hydrogen bonding and cation-dipole attraction in montmorillonite (Mooney et al., 1952a, 1952b). According to Table 2, the 7R gray shale has the smallest C value and thus the smallest intermolecular bonding between water molecules and mineral surfaces.

The GAB monolayer adsorption V_m for all five tested samples are also listed in Table 2. V_m shows the same sequence with the amount of water vapor adsorption at lower R_h values in the order: H6 > 6F > 6R > 5A > 7R. Particularly, H6 shale containing expansive montmorillonite presents the highest V_m, which is attributed to the significant contribution of cation hydration and clay swelling at higher R_h values (Arthur et al., 2018). The relatively large monolayer capacity directly corresponds to a large SSA. The SSA obtained from water adsorption, and its difference to the SSA obtained from N_2 adsorption is discussed later in section 3.5. Additionally, for the four illite-rich shale samples, that is, 6R, 5A, 7R, and 6F, the critical R_h at which monolayer coverage completes at 0.37, 0.32, 0.34, and 0.25, respectively. These values are approximately consistent with a study by (Newman, 1983) that monolayer coverage for non-swelling clays is completed at the critical R_h of 0.47 divided by a correction factor 1.7. For H6 shale containing montmorillonite, the critical R_h is 0.39, which is smaller than the critical R_h (0.47) for swelling clays reported in the study (Newman, 1983) but similar to that (0.34) reported in another study (Arthur et al., 2018).

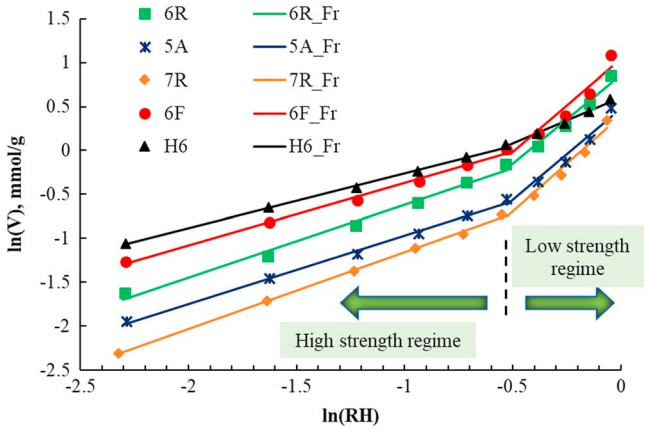

Figure 7. Adsorption isotherms for the five shale samples at 30 °C recovered from linear fits of the Freundlich model. Note the two distinct linear regions and the critical R_h value at the inflection point (R_h ~0.6).

3.3.2. Freundlich Modeling Analysis

The experimental data for the five shale samples show two distinct linear regions (Figure 7) when plotting them in the linear form of the Freundlich model (see the details in the Appendix A2). The two distinct linear regions can be fitted by the Freundlich model separately with the corresponding Freundlich constants k and n presented in Table 3. Variable k represents water adsorption capacity with n, the reciprocal of the slope of the plot of $\mathbf{ln}\boldsymbol{V}$ versus $\mathbf{ln}\boldsymbol{R_h}$, represents the adsorption strength. The two distinct regions represent two different adsorption regimes, depending on the

Table 3
Freundlich Modeling Parameters of Adsorption Isotherms of the Five Shale Samples at 30 °C

Model type	Shale type	Model coefficients k	n	RH_c[a]	Goodness of fit indexes SSE	R^2	RMSE
Freundlich k, n	6R	1.24	1.20	~0.6	1.71E−2	0.989	6.54E−2
		2.37	0.49		1.88E−2	0.970	7.92E−2
	5A	0.83	1.28		5.40E−3	0.996	3.67E−2
		1.61	0.48		2.57E−2	0.961	9.25E−2
	7R	0.75	1.14		2.00E−3	0.999	2.25E−2
		1.48	0.46		2.32E−2	0.967	8.80E−2
	6F	1.41	1.40		5.90E−3	0.995	3.83E−2
		2.82	0.47		4.88E−2	0.930	1.28E−1
	H6	1.45	1.59		2.00E−3	0.998	2.23E−2
		1.84	0.94		1.80E−3	0.989	2.48E−2

Note. RMSE = root-mean-square error.
[a]RH_c refers to the critical R_h at which the transition of the two distinct regimes occurs for Freundlich fit.

value of n: a high adsorption strength regime at low R_h values and a low adsorption strength regime at high R_h, with a transitional relative humidity of RH_c ~0.6. The presence of twin adsorption regimes recovered from the Freundlich model has been observed in previous studies of water adsorption on clay minerals (Feng et al., 2018; Hatch et al., 2012; Zhang et al., 2016). This model is capable of describing experimental adsorption data at a broad range of R_h values.

In the stronger adsorption regime ($R_h < 0.6$), a similar trend of k with the trend of monolayer capacity V_m (Table 2) is observed as H6 > 6F > 6R > 5A > 7R. For the weaker adsorption regime ($R_h > 0.6$), k values of the five shales have the following trend: 6F > 6R > H6 > 5A > 7R. This is consistent with the ordered trend of the sorption isotherms for the five shale samples. Therefore, the Freundlich constant k predictively represents the water adsorption capacity in both strong and weak adsorption regimes.

From Table 3, the values of n for all shale samples are greater than unity at low R_h, suggesting a strong affinity to water vapor. Conversely, the n values at high R_h are smaller than unity, indicating a weaker affinity to water vapor. For the stronger adsorption regime ($R_h < 0.6$), the H6 black shale presents the strongest adsorption strength ($n = 1.59$), followed by the 6F black shale ($n = 1.4$), and the sample 5A ($n = 1.28$), 6R ($n = 1.20$), and 7R ($n = 1.14$) gray shales. This is consistent with the parameter C, recovered from the GAB analysis, indicating again that the two black shales show stronger adsorption strength, which is possibly due to the presence of kerogen containing hydrophilic carbonyl and hydroxyl groups (6F shale) and/or montmorillonite (H6 shale) containing interlayer exchangeable cations.

From Table 3, in the weaker adsorption regime ($R_h > 0.6$), the H6 black shale retains a stronger adsorption strength (n =0.94) than the other four shale samples (n = ~0.5). As suggested by the X-ray diffraction patterns of montmorillonite during hydration (Cases et al., 1992), two or three water sheets can be formed in the interlamellar spaces at R_h magnitudes between 0.5 and 0.93. Therefore, cation-dipole attraction may still contribute to a stronger adsorption strength of the H6 black shale in the weaker adsorption regime (R_h > 0.6). As observed in Figure 7, the amount of water adsorption at R_h ~0.95 deviates upwards from the low adsorption regime curve, indicating a lower adsorption strength (smaller n value) at this R_h. This can be attributed to the predominance of condensation effects in the mesopores, resulting in a reduced adsorption strength due to the only weak dipole-dipole interaction between water molecules.

3.4. Isosteric Heat of Sorption

Sorption isotherms of the five shales are temperature dependent (Figure 8)—water vapor adsorption on samples 6R, 5A, 7R, and 6F under different humidity environments are negatively correlated with temperature. Higher temperature tends to enhance the excitation of water molecules, reduce the intermolecular distance, and reduce the interaction energy between water molecules and solid surfaces. Consequently, water molecules are unstable at higher temperature and tend to be desorbed from the adsorption sites, causing the reduction of equilibrium moisture content at a specific R_h value due to the decrease of mutual attractive forces. The isosteric heat of adsorption is one of the most fundamental thermodynamic quantities to describe the energy of interaction or intermolecular bonding between water molecules and solid surfaces (Myers, 2002). Figure 9 presents the water vapor adsorption as a function of vapor pressure (p) at different temperatures (T) along with plots of $\mathbf{ln(}\boldsymbol{p}\mathbf{)}$ against $\mathbf{(1/}\boldsymbol{T}\mathbf{)}$ for sample 6R. For a specific vapor pressure, ΔH_{ads} values can be deduced from the slope of the plot $\mathbf{ln(}\boldsymbol{p}\mathbf{)}$ against $\mathbf{1/}\boldsymbol{T}$ via the Clausius-Clapeyron equation (equation (B1) in Appendix B).

The isosteric heats of adsorption (ΔH_{ads}) for the tested shale samples (Figure 10) are negative, ranging from ~44 to 54 kJ/mole at a water adsorption of ~0.1–1.8 mmol/g, and as such represents an exothermic process. The heat of adsorption for the tested shales decreases smoothly with increased water content and progressively approaches the latent heat (ΔH_{H_2O}) of vaporization of pure water at ~30 °C. This can be attributed to a continuous distribution of the binding sites for water adsorption. At low R_h, water molecules adsorb

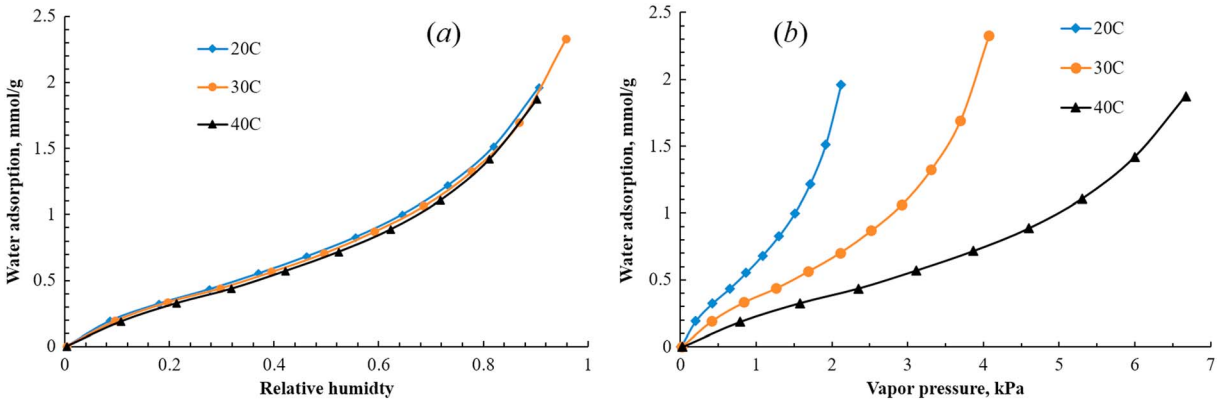

Figure 8. Effect of temperature on water adsorption on sample 6R as a function of R_h (a) and partial pressure (b) of water vapor.

on the more active sites where there is stronger intermolecular bonding between water molecules and solid surfaces. As R_h increases to the relative higher values, water molecules adsorb in the less active sites and multilayer adsorption occurs. At high R_h values, vapor condensation in capillary pores dominates which is associated with a weak dipole-dipole interaction between water molecules. In other words, adsorption will occur initially at the most active sites with the highest interaction energy released. As R_h increases, adsorption/condensation gradually occurs at the less active sites with lower interactive energies released (McLaughlin & Magee, 1998). No distinct transition from monolayer to multilayer and to capillary condensation is observed since monolayer/multilayer adsorption on more flat surfaces and condensation in smaller capillaries can occur simultaneously at different pore sites (Allardice & Evans, 1971). The observation that the values of ΔH_{ads} are larger than ΔH_{H_2O} also indicates that intermolecular bonding between water molecules and the sorption sites is higher than that between water molecules of the condensed pure water (Masuzawa & Sterling, 1968). A similar trend has been reported for water vapor adsorption on sodium montmorillonite (Mooney et al., 1952a), Marcellus shale (Tang et al., 2017), lignite (Wan et al., 2016), and on foods (Quirijns et al., 2005).

Among the five shale samples, sample H6 presents the highest isosteric heat of adsorption followed by samples 6F and 6R, while samples 5A and 7R present the least. This is overall consistent with the GAB analysis and the Freundlich analysis described in section 3.3. Besides, sample H6 (black shale) presents a higher isosteric heat of adsorption than vaporization of pure water at high water content, consistent with the Freundlich analysis. This can be attributed to hydration in the interlamellar space of the montmorillonite at high R_h values (Cases et al., 1997; Ferrage et al., 2010; Mooney et al., 1952b) where a relatively higher interaction energy is maintained due to a strong cation-dipole attraction.

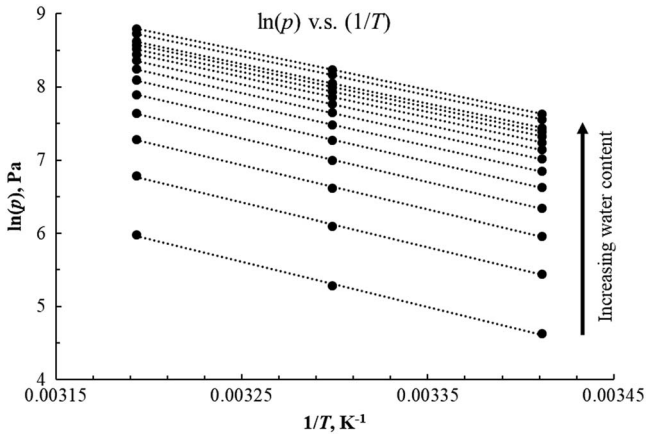

Figure 9. Isosteric curves of sample 6R at various water contents from 0.1–1.8 mmol/g.

3.5. Comparison of N_2-SSA and H_2O-SSA

The SSAs of the five shale samples can be calculated from the water adsorption isotherms by multiplying the number of monolayer water molecules by the cross-sectional area of a single water molecule (10.6 $Å^2$; Newman, 1983). A comparison of SSAs of the five shale samples evaluated from both N_2 and water adsorption is shown in Figure 11. SSAs recovered from water adsorption are larger than those recovered by N_2 adsorption for all samples. Presumably, the adsorption of water and nitrogen occupy the same surface sites if we consider merely Van der Waals force and ignore the size effect of water molecule and nitrogen molecule. However, due to the polarity of water molecules, a complex surface chemistry (Seemann et al., 2017; Thommes et al., 2013) can cause greater water adsorption than N_2 adsorption at the same relative pressure, since the intermolecular bonding between water molecules and shale surfaces (such as hydrogen bonding and ion-dipole attraction) are much higher than the Van der Waals forces between shale surfaces and nitrogen

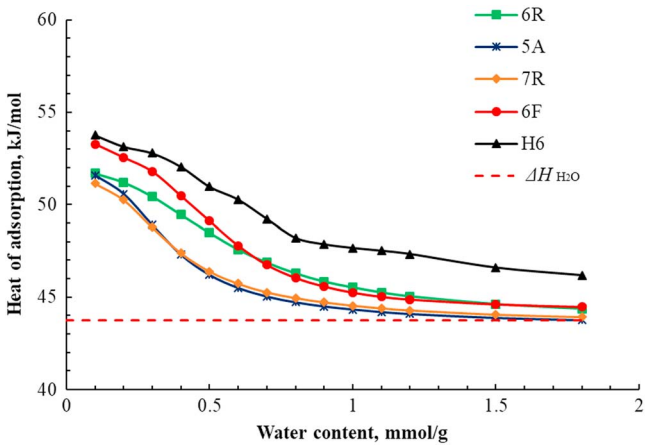

Figure 10. Isosteric heat of adsorption as a function of water content for the tested shales. The latent heat (ΔH_{H_2O}) of vaporization of pure water at ~30 °C is also shown (horizontal red dashed line).

molecules (Mooney et al., 1952a). This can lead to a larger monolayer coverage "area" for water molecules where nitrogen molecules cannot be adsorbed, due to smaller Van der Waals forces. Particularly, for expansive clay minerals, such as montmorillonite containing multiscale pore structures, the "internal" interlamellar pore spaces are inaccessible to nitrogen molecules (Aylmore & Quirk, 1967; Diamond & Kinter, 1956; Hendricks et al., 1940; Mooney et al., 1952a) due to the lack of cation-dipole attraction. Water molecules, however, can be adsorbed by the exchangeable cations in these interlamellar spaces (<2 nm) of the two sandwiched layers. This is due to the cation-dipole attraction inducing a remarkable increase of interlayer distance, known as clay swelling, which in turn contributes significantly to water adsorption (Hatch et al., 2012; Hendricks et al., 1940; Mooney et al., 1952b). Additionally, water can also be adsorbed on the external surfaces, interparticle mesoporous spaces (2-50 nm) and macroporous spaces between aggregates (>50 nm; Cases et al., 1992; Ferrage et al., 2005; Salles et al., 2010). As expected, among all the shale samples, sample H6 containing 8.6% montmorillonite records an "abnormally" largest H_2O SSA despite having the smallest N_2 SSA (8.9 m^2/g), as is shown in Figure 11. The inaccessible porosity/SSA of sample H6 (black shale) has also been justified by small angle neutron scattering (SANS) measurements capable of detecting the pore spaces inaccessible to N_2 molecules (Sang et al., 2018).

3.6. Role of Mesopore Condensation

Based on Kelvin equation, the ratio of capillary water in mesopores (2–50 nm) to the measured water adsorption at different R_h (Figure 12) was estimated through the pore size distributions for the five shales, which were obtained by the low pressure N_2 adsorption experiment from adsorption branches (see supporting information Figure S1). Figure 12 shows that mesopore condensation contributes increasingly to the total water adsorption as R_h increases. For the four shale samples (6R, 5A, 7R, and 6F), mesopore condensation at $R_h < 0.4$ is insignificant while it starts to dominate at $R_h > 0.9$. The low contribution of mesopore condensation to total water adsorption at $R_h < 0.4$ can be attributed to the dominant roles of particle surface hydration and/or cation hydration which are mainly controlled by surface forces, cation capacity and types. For H6 shale, the contribution of mesopore condensation is lower than ~33% throughout the entire measured range of R_h (0–0.95). There are two possible explanations. On the one hand, condensation in mesopores is limited due to the small external mesopores, as indicated by N_2 adsorption (Figure 5b) and MIP results (Figure 6b). On the other hand, interlayer cation hydration in montmorillonite and induced-swelling play an important role in total water adsorption throughout the measured R_h range, leaving the less dominant role of capillary condensation in mesopores. This is also consistent with previous modeling analyses and analysis of heat of sorption that the interaction energy for H6 shale at high R_h values is still relatively strong compared to other samples. Note that sorption thickness is neglected in this study, which may lead to a slight underestimation of the mesopore condensation based on Kelvin equation (Barrett et al., 1951). Besides, due to the limitation of low pressure N_2 adsorption, which only characterizes pores larger than 1.7 nm based on BJH adsorption branch, micropore filling and condensation in large micropores (smaller than but close to 2 nm) are not considered in this study.

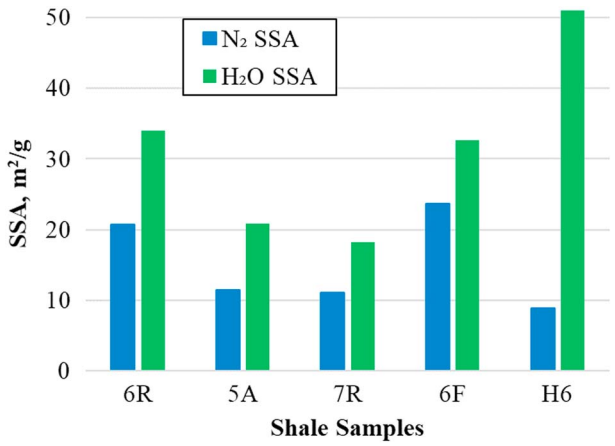

Figure 11. SSAs of the five shale samples obtained from low-pressure N_2 adsorption at −196 °C (77 K), and SSAs obtained from water vapor adsorption (green bar) at 30 °C. SSA = specific surface area.

3.7. Role of Clay Minerals and Kerogen

For shales containing nonexpansive clay minerals, such as kaolinite and illite, layer-by-layer adsorption followed by vapor condensation at high R_h is a satisfactory model for water vapor adsorption behavior (Feng et al., 2018; Hatch et al., 2012; Schuttlefield et al., 2007). Hydration in shales containing expansive montmorillonite, however, may not follow

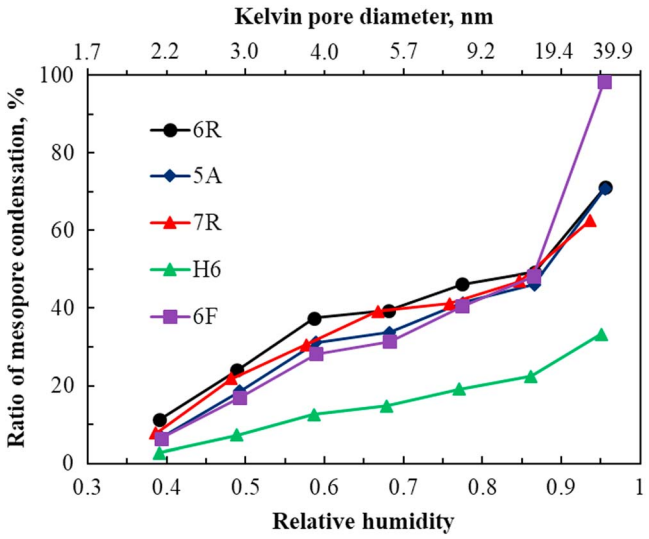

Figure 12. Ratios of mesopore (2–50 nm) condensation based on Kelvin equation to measured water adsorption at different R_h values for the five shale samples at 30 °C.

this conventional trend. This is because hydration in montmorillonite is fundamentally different to that for nonexpansive kaolinite and illite. At R_h values below 0.1-0.2, monolayer molecular hydration occurs on the "external" particle/pore surfaces (Keren & Shainberg, 1975; Salles et al., 2008). At higher R_h values, multilayer adsorption of water vapor in these "external" particle/pore surfaces begins and capillary condensation in mesopores then occurs with the further increase of R_h values. Concomitantly, water molecules also start to hydrate on the "internal" surfaces and/or at the interlayer cations to form a discrete number (typically 1 or 2) of interlayer water sheets (Cases et al., 1992; Ferrage et al., 2005; Salles et al., 2008). This results in a remarkable interlamellar swelling which in turn contributes to further water adsorption and/or condensation at high R_h values (Hatch et al., 2012; Hendricks et al., 1940; Mooney et al., 1952b). Therefore, water adsorption on shale containing expansive clays involves a complex interlayer cation hydration process, which may not be fully represented by monolayer/multilayer sorption and capillary condensation in shales containing only nonexpansive clays.

Shale organic kerogen, especially for low thermal maturity kerogen, may also play an important role in shale hydration. This is due to its potential of containing a large number of micropores/mesopores (Liu et al., 2019) and hydrophilic functional groups (Hu et al., 2014, 2016). As measured by X-ray Photoelectron Spectroscopy, the functionalized oxygen-to-carbon (O/C) atomic ratio for 6F shale comes to 20.4%, which is much higher than that for H6 shale (only 5.0%). This high functionalized oxygen-containing functional groups together with the high porosity, as characterized by N_2 sorption and MIP intrusion, could lead to a relatively high water sorption capacity for 6F shale than other shales (Figure 4). Figure 13 shows a schematic of the water adsorption process in kerogen containing both hydrophilic and hydrophobic sites. For hydrophilic sites, water molecules absorb on the surfaces of oxygen-containing groups through hydrogen bonding at low R_h values. These form clusters on the preadsorbed molecules or condense in these hydrophilic pores at high R_h values (Charrière & Behra, 2010; Mahajan & Walker, 1971; McCutcheon et al., 2003; Švábová et al., 2011). Therefore, hydrophilic pores in kerogen can contribute to the total amount of hydration in organic-rich shales. For hydrophobic sites, the lack of hydrogen bonding with functional groups causes almost no water adsorption at low R_h values, since intermolecular interaction between water molecules and the surface is less than the mutual water-water interaction. Though there is negligible water adsorption on these hydrophobic pores at low R_h values, water clustering may still occur

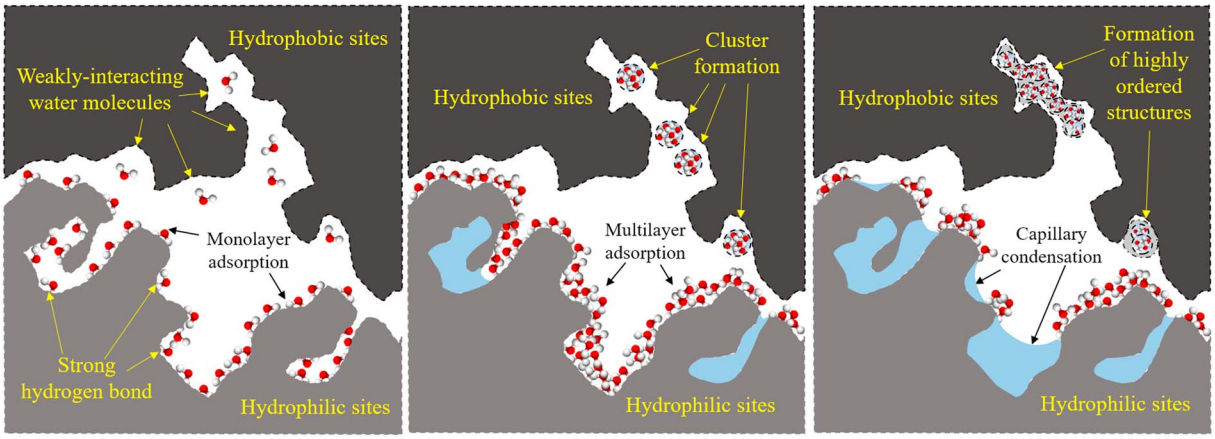

Figure 13. Schematic of water adsorption mechanisms in organic matter within shale containing both hydrophilic (functional groups) and hydrophobic sites. For hydrophilic sites, monolayer adsorption occurs at low R_h, due to strong hydrogen bonding, and condensation dominates at high R_h with weak dipole-dipole attraction. For hydrophobic sites, water clustering, and condensation may occur at very high R_h (Cailliez et al., 2008; Kimura et al., 2004).

in these hydrophobic pores at high R_h values (Cailliez et al., 2008; Kimura et al., 2004). In this sense, hydrophobic pores in kerogen may also contribute to a certain degree to the total amount of hydration in organic-rich shales. Water vapor adsorption in pure kerogen plays a significant role during gas extraction in gas shale reservoirs because methane will compete with water vapor for both adsorption and diffusion (Wang et al., 2011). In this study, we can only measure and quantify the combined water vapor adsorption for all the shale compositions and it is not feasible to quantify the relative contribution for each constituent of the shale. Certainly, further studies will be required to characterize and quantify the pure kerogen water adsorption behavior under in situ reservoir conditions.

4. Conclusions

Water vapor ad/desorption experiments are conducted for three gray shales (6R, 5A, and 7R) and two black shales (6F and H6) from Illinois basin at various temperatures (20, 30, and 40 °C) and R_h (0 to 0.95) using DVS method. GAB and Freundlich models are applied to model the hydration mechanisms of the shale samples over the entire R_h ranges. Shale hydration under different humidities is found to be closely related to both surface chemistry and pore structure. The principal findings are summarized as follows.

Water vapor adsorption on the five shales is by pure physisorption. Layer-by-layer adsorption followed by capillary condensation explains the observed water vapor sorption behavior on the shales containing no expansive clays. At low R_h, water molecules initially adsorb on active shale particle/pore surfaces with high isosteric heat of sorption, influenced by mineral surfaces, cation types, and functional groups. At very high R_h (>0.9), capillary condensation in mesopores starts to dominate and is mainly determined by the pore structure. For shales containing montmorillonite, however, interlayer cation hydration and clay swelling cannot be neglected.

The GAB model and the Freundlich model can describe the adsorption isotherms over the entire range of R_h. The Freundlich model reveals a strong adsorption strength at lower R_h (<0.6) and a weak adsorption strength at high R_h (>0.6).

Overall, the SSA measured by water adsorption is larger than that recovered from N_2 adsorption—due to the complex surface chemistry occurring for water adsorption at low R_h values. For sample H6, containing expansive montmorillonite, many interlayer voids/spaces in the montmorillonite are accessible to water but inaccessible to N_2 molecules. This results in a much larger SSA measured by water than that by N_2. Despite this higher water adsorption at low R_h values (<0.6) due to the large amount of interlayer spaces, the amount of water condensation can still be limited at high R_h values due to its small external pore volume.

Among the four shales containing no expansive clays, kerogen with high oxygen-containing functional groups may lead to an overall higher water adsorption capacity for one organic-rich shale.

Appendix A: Water Sorption Isotherm Models

A1. GAB Model

The GAB model (Anderson, 1946; de Boer, 1953; Guggenheim, 1966) is an extension of the BET theory (Brunauer et al., 1938) and is applicable over a more broad range of relative humidity. BET theory assumes that the heat of adsorption after the completion of the monolayer is equal to the heat of liquefaction, whereas the GAB model assumes that the heat of adsorption of the second and/or higher multilayers is less than the heat of liquefaction, implying that molecules of the sorbate beyond monolayer adsorption continues to be interacted with the sorbent surface. GAB equation introduces an additional parameter K in the following expression.

$$V = \frac{V_m K C R_h}{(1-KR_h)[1-KR_h + CKR_h]} \tag{A1}$$

where V_m and C are analogous to that in the BET equation, representing monolayer adsorption and a constant related to heat of adsorption, respectively; K is a correction factor, quantifying the potential of multilayer molecules relative to the potential of bulk liquid.

A2. Freundlich Sorption Model

The Freundlich model (Freundlich, 1932) is an empirical model to represent sorption on heterogeneous sorbents. Unlike the Langmuir model, the amount of adsorbed water is absent of a plateau at high R_h. Also, the adsorption rate of water at high R_h is much smaller than the BET model (Do, 1998), which is functionally unlimited. The linear form of the Freundlich model is defines as

$$\ln V = \ln k + \frac{1}{n}\ln R_h \tag{A2}$$

where V is the sorbed volume; k and n are the Freundlich empirical constants recovered from regression of the adsorption data and representing the sorption capacity and sorption strength, respectively.

A3. Error Analysis

Three indexes were calculated to evaluate the accuracy in the fitting of results: the sum of squares of the error (SSE), the maximum degrees of freedom correlation coefficient squared (R^2), and the root-mean-square error (RMSE). The SSE measures the total deviation of the experimental values from the fitted values; R^2 measures how well the fit explains the variation of the data; and RMSE is an estimate of the standard deviation of the random component in the data. These three indexes are mathematically given by the following equations.

$$SSE = \sum_{i=1}^{m} w_i (y_i - \widehat{y}_i)^2 \tag{A3}$$

$$R^2 = 1 - \frac{\sum_{i=1}^{m} (y_i - \widehat{y}_i)^2}{\sum_{i=1}^{m} (y_i - \bar{y}_i)^2} \tag{A4}$$

$$RMSE = \left[\frac{1}{m}\sum_{i=1}^{m} (y_i - \widehat{y}_i)\right]^{1/2} \tag{A5}$$

where $y_i, \widehat{y}_i$, and $\bar{y}_i$ are the experimental data, the fitted value and the mean of experimental data respectively. Variable m is the number of data samples. For all models, lower values of SSE and RMSE and higher value of R^2 indicate a better regression quality.

Appendix B: Isosteric Heat of Water Vapor Sorption

The differential enthalpy of the system (ΔH_{ads}) due to adsorption at a particular sorption site, known as the isosteric heat of adsorption, plays an important role in describing the strength of the interaction between water vapor molecules and adsorbent. This is a measure of the intermolecular bonding between water molecules and sorbent surfaces. Assuming that the isosteric heat of adsorption is temperature independent, the Clausius-Clapeyron equation allows the estimation of the heat of adsorption ΔH_{ads} as

$$\left[\frac{\partial \ln(p)}{\partial (1/T)}\right]_V = -\frac{1}{R}\Delta H_{ads} \tag{B1}$$

where p is the partial pressure of the water vapor (kPa); T is the temperature (K), and R is the universal gas constant ($J \cdot mol^{-1} \cdot K^{-1}$); and ΔH_{ads} is the heat of adsorption at a specific water content V (mmol/g). The heat of adsorption ΔH_{ads} can be calculated from the linearized plot of $\mathbf{ln}\boldsymbol{P}$ versus $(\mathbf{1}/\boldsymbol{T})$ over a given moisture content range. Typically, the slope of this ln(p)-versus-(1/T) is negative, defining ΔH_{ads} as negative and prescribing that water adsorption is an exothermic process.

Acknowledgments
This work is financially supported by The National Institute of Occupational Safety and Health (NIOSH) under the Contract NIOSH-200-2016-90385. The authors also want to thank Yu Liu from China University of Mining and Technology for the discussions and suggestions for this paper. Three anonymous reviewers and the Associate Editor are also appreciated for the valuable comments and suggestions. The data used in this paper can be downloaded from the Zenodo website (https://zenodo.org/record/3359256).

References

Akin, I. D., & Likos, W. J. (2014). Specific surface area of clay using water vapor and EGME sorption methods. *Geotechnical Testing Journal*, *37*(6), 1016–1027.

Allardice, D. J., & Evans, D. G. (1971). The-brown coal/water system: Part 2. Water sorption isotherms on bed-moist Yallourn brown coal. *Fuel*, *50*(3), 236–253. https://doi.org/10.1016/0016-2361(71)90014-7

Anderson, R. B. (1946). Modifications of the Brunauer, Emmett and Teller equation. *Journal of the American Chemical Society*, *68*(4), 686–691. https://doi.org/10.1021/ja01208a049

Arthur, E., Tuller, M., Moldrup, P., & de Jonge, L. W. (2016). Evaluation of theoretical and empirical water vapor sorption isotherm models for soils. *Water Resources Research*, *52*, 190–205. https://doi.org/10.1002/2015WR017681

Arthur, E., Tuller, M., Moldrup, P., Greve, M. H., Knadel, M., & de Jonge, L. W. (2018). Applicability of the Guggenheim–Anderson–Boer water vapour sorption model for estimation of soil specific surface area. *European Journal of Soil Science*, *69*(2), 245–255.

Aylmore, L. A. G., & Quirk, J. P. (1967). The micropore size distributions of clay mineral systems. *Journal of Soil Science*, *18*(1), 1–17. https://doi.org/10.1111/j.1365-2389.1967.tb01481.x

Barrett, E. P., Joyner, L. G., & Halenda, P. P. (1951). The determination of pore volume and area distributions in porous substances. I. Computations from nitrogen isotherms. *Journal of the American Chemical Society*, *73*(1), 373–380.

Bérend, I., Cases, J.-M., François, M., Uriot, J.-P., Michot, L., Masion, A., & Thomas, F. (1995). Mechanism of adsorption and desorption of water vapor by homoionic montmorillonites: 2. The Li+ Na+, K+, Rb+ and Cs+-exchanged forms. *Clays and Clay Minerals*, *43*(3), 324–336. https://doi.org/10.1346/CCMN.1995.0430307

Brunauer, S., Emmett, P. H., & Teller, E. (1938). Adsorption of gases in multimolecular layers. *Journal of the American Chemical Society*, *60*(2), 309–319. https://doi.org/10.1021/ja01269a023

Busch, A., Alles, S., Gensterblum, Y., Prinz, D., Dewhurst, D. N., Raven, M. D., et al. (2008). Carbon dioxide storage potential of shales. *International Journal of Greenhouse Gas Control*, *2*(3), 297–308. https://doi.org/10.1016/j.ijggc.2008.03.003

Cailliez, F., Stirnemann, G., Boutin, A., Demachy, I., & Fuchs, A. H. (2008). Does water condense in hydrophobic cavities? A molecular simulation study of hydration in heterogeneous nanopores. *The Journal of Physical Chemistry C*, *112*(28), 10,435–10,445. https://doi.org/10.1021/jp710746b

Cases, J. M., Bérend, I., Besson, G., Francois, M., Uriot, J. P., Thomas, F., & Poirier, J. E. (1992). Mechanism of adsorption and desorption of water vapor by homoionic montmorillonite. 1. The sodium-exchanged form. *Langmuir*, *8*(11), 2730–2739. https://doi.org/10.1021/la00047a025

Cases, J. M., Bérend, I., François, M., Uriot, L. P., Michot, L. J., & Thomas, F. (1997). Mechanism of adsorption and desorption of water vapor by homoionic montmorillonite: 3. The Mg 2+, Ca 2+, Sr 2+ and Ba 2+ exchanged forms. *Clays and Clay Minerals*, *45*(1), 8–22. https://doi.org/10.1346/CCMN.1997.0450102

Charrière, D., & Behra, P. (2010). Water sorption on coals. *Journal of Colloid and Interface Science*, *344*(2), 460–467. https://doi.org/10.1016/j.jcis.2009.11.064

Chen, G., Chenevert, M. E., Sharma, M. M., & Yu, M. (2003). A study of wellbore stability in shales including poroelastic, chemical, and thermal effects. *Journal of Petroleum Science and Engineering*, *38*(3–4), 167–176. https://doi.org/10.1016/S0920-4105(03)00030-5

Chugh, Y. P., & Missavage, R. A. (1981). Effects of moisture on strata control in coal mines. *Engineering Geology*, *17*(4), 241–255. https://doi.org/10.1016/0013-7952(81)90001-6

Clarkson, C. R., Solano, N., Bustin, R. M., Bustin, A. M. M., Chalmers, G. R. L., He, L., et al. (2013). Pore structure characterization of North American shale gas reservoirs using USANS/SANS, gas adsorption, and mercury intrusion. *Fuel*, *103*, 606–616. https://doi.org/10.1016/j.fuel.2012.06.119

Curtis, J. B. (2002). Fractured shale-gas systems. *AAPG Bulletin*, *86*(11), 1921–1938.

de Boer, J. H. (1953). *The dynamical character of adsorption*. Oxford: Oxford University Press.

Derjaguin, B. V. (1992). Some results from 50 years' research on surface forces. *Progress in Surface Science*, *40*(1–4), 240–251. https://doi.org/10.1016/0079-6816(92)90051-I

Diamond, S., & Kinter, E. B. (1956). Surface areas of clay minerals as derived from measurements of glycerol retention. *Clays and Clay Minerals*, *5*(1), 334–347. https://doi.org/10.1346/CCMN.1956.0050128

Do, D. D. (1998). *Adsorption analysis: Equilibria and kinetics* (Vol. 2). London: Imperial College Press.

Dubinin, M. (1960). The potential theory of adsorption of gases and vapors for adsorbents with energetically nonuniform surfaces. *Chemical Reviews*, *60*(2), 235–241. https://doi.org/10.1021/cr60204a006

Elsworth, D., Spiers, C. J., & Niemeijer, A. R. (2016). Understanding induced seismicity. *Science*, *354*(6318), 1380–1381. https://doi.org/10.1126/science.aal2584

Feng, D., Li, X., Wang, X., Li, J., Sun, F., Sun, Z., et al. (2018). Water adsorption and its impact on the pore structure characteristics of shale clay. *Applied Clay Science*, *155*, 126–138. https://doi.org/10.1016/j.clay.2018.01.017

Ferrage, E., Lanson, B., Michot, L. J., & Robert, J.-L. (2010). Hydration properties and interlayer organization of water and ions in synthetic Na-smectite with tetrahedral layer charge. Part 1. Results from X-ray diffraction profile modeling. *The Journal of Physical Chemistry C*, *114*(10), 4515–4526. https://doi.org/10.1021/jp909860p

Ferrage, E., Lanson, B., Sakharov, B. A., & Drits, V. A. (2005). Investigation of smectite hydration properties by modeling experimental X-ray diffraction patterns: Part I. Montmorillonite hydration properties. *American Mineralogist*, *90*(8–9), 1358–1374. https://doi.org/10.2138/am.2005.1776

Freundlich, H. (1932). Of the adsorption of gases. Section II. Kinetics and energetics of gas adsorption. Introductory paper to section II. *Transactions of the Faraday Society*, *28*, 195–201.

Gautschi, A. (2001). Hydrogeology of a fractured shale (Opalinus Clay): Implications for deep geological disposal of radioactive wastes. *Hydrogeology Journal*, *9*(1), 97–107. https://doi.org/10.1007/s100400000117

Gregg, S. J., Sing, K. S. W., & Salzberg, H. W. (1967). Adsorption surface area and porosity. *Journal of the Electrochemical Society*, *114*(11), 279C–279C. https://doi.org/10.1149/1.2426447

Guggenheim, E. A. (1966). *Applications of statistical mechanics*. London: Oxford University Press.

Guiltinan, E. J., Cardenas, M. B., Bennett, P. C., Zhang, T., & Espinoza, D. N. (2017). The effect of organic matter and thermal maturity on the wettability of supercritical CO_2 on organic shales. *International Journal of Greenhouse Gas Control*, *65*, 15–22. https://doi.org/10.1016/j.ijggc.2017.08.006

Gutierrez-Rodriguez, J. A., Purcell, R. J. Jr., & Aplan, F. F. (1984). Estimating the hydrophobicity of coal. *Colloids and Surfaces*, *12*, 1–25. https://doi.org/10.1016/0166-6622(84)80086-4

Hatch, C. D., Wiese, J. S., Crane, C. C., Harris, K. J., Kloss, H. G., & Baltrusaitis, J. (2012). Water adsorption on clay minerals as a function of relative humidity: Application of BET and Freundlich adsorption models. *Langmuir*, *28*(3), 1790–1803. https://doi.org/10.1021/la2042873

Hendricks, S. B., Nelson, R. A., & Alexander, L. T. (1940). Hydration mechanism of the clay mineral montmorillonite saturated with various Cations1. *Journal of the American Chemical Society*, *62*(6), 1457–1464. https://doi.org/10.1021/ja01863a037

Hu, Y., Devegowda, D., & Sigal, R. (2016). A microscopic characterization of wettability in shale kerogen with varying maturity levels. *Journal of Natural Gas Science and Engineering*, *33*, 1078–1086. https://doi.org/10.1016/j.jngse.2016.06.014

Hu, Y., Devegowda, D., Striolo, A., Phan, A., Ho, T. A., Civan, F., & Sigal, R. F. (2014). Microscopic dynamics of water and hydrocarbon in shale-kerogen pores of potentially mixed wettability. *SPE Journal*, *20*(01), 112–124. https://doi.org/10.2118/167234-PA

Jackson, R. B., Vengosh, A., Darrah, T. H., Warner, N. R., Down, A., Poreda, R. J., et al. (2013). Increased stray gas abundance in a subset of drinking water wells near Marcellus shale gas extraction. *Proceedings of the National Academy of Sciences*, *110*(28), 11,250–11,255. https://doi.org/10.1073/pnas.1221635110

Katz, S. M. (1949). Permanent hysteresis in physical adsorption. A theoretical discussion. *The Journal of Physical Chemistry*, *53*(8), 1166–1186. https://doi.org/10.1021/j150473a003

Keren, R., & Shainberg, I. (1975). Water vapor isotherms and heat of immersion of Na/Ca-montmorillonite systems—I: Homoionic clay. *Clays and Clay Minerals*, *23*(3), 193–200. https://doi.org/10.1346/CCMN.1975.0230305

Khorshidi, M., Lu, N., Akin, I. D., & Likos, W. J. (2017). Intrinsic relationship between specific surface area and soil water retention. *Journal of Geotechnical and Geoenvironmental Engineering*, *143*(1), 04016078. https://doi.org/10.1061/(ASCE)GT.1943-5606.0001572

Kimura, T., Kanoh, H., Kanda, T., Ohkubo, T., Hattori, Y., Higaonna, Y., et al. (2004). Cluster-associated filling of water in hydrophobic carbon micropores. *The Journal of Physical Chemistry B*, *108*(37), 14,043–14,048. https://doi.org/10.1021/jp048934n

Li, J., Li, X., Wu, K., Wang, X., Shi, J., Yang, L., et al. (2016). Water sorption and distribution characteristics in clay and shale: Effect of surface force. *Energy & Fuels*, *30*(11), 8863–8874. https://doi.org/10.1021/acs.energyfuels.6b00927

Liu, S., Zhang, R., Karpyn, Z., Yoon, H., & Dewers, T. (2019). Investigation of accessible pore structure evolution under pressurization and adsorption for coal and shale using small-angle neutron scattering. *Energy & Fuels*, *33*(2), 837–847.

Lu, N., & Khorshidi, M. (2015). Mechanisms for soil-water retention and hysteresis at high suction range. *Journal of Geotechnical and Geoenvironmental Engineering*, *141*(8), 04015032. https://doi.org/10.1061/(ASCE)GT.1943-5606.0001325

Macht, F., Eusterhues, K., Pronk, G. J., & Totsche, K. U. (2011). Specific surface area of clay minerals: Comparison between atomic force microscopy measurements and bulk-gas (N2) and-liquid (EGME) adsorption methods. *Applied Clay Science*, *53*(1), 20–26. https://doi.org/10.1016/j.clay.2011.04.006

Mahajan, O. P., & Walker, P. L. Jr. (1971). Water adsorption on coals. *Fuel*, *50*(3), 308–317. https://doi.org/10.1016/0016-2361(71)90019-6

Masuzawa, M., & Sterling, C. (1968). Gel–water relationships in hydrophilic polymers: Thermodynamics of sorption of water vapor. *Journal of Applied Polymer Science*, *12*(9), 2023–2032. https://doi.org/10.1002/app.1968.070120904

McCutcheon, A. L., Barton, W. A., & Wilson, M. A. (2003). Characterization of water adsorbed on bituminous coals. *Energy & Fuels*, *17*(1), 107–112. https://doi.org/10.1021/ef020101d

McLaughlin, C. P., & Magee, T. R. A. (1998). The determination of sorption isotherm and the isosteric heats of sorption for potatoes. *Journal of Food Engineering*, *35*(3), 267–280. https://doi.org/10.1016/S0260-8774(98)00025-9

Michot, L. J., Bihannic, I., Pelletier, M., Rinnert, E., & Robert, J.-L. (2005). Hydration and swelling of synthetic Na-saponites: Influence of layer charge. *American Mineralogist*, *90*(1), 166–172. https://doi.org/10.2138/am.2005.1600

Mooney, R. W., Keenan, A. G., & Wood, L. A. (1952a). Adsorption of water vapor by Montmorillonite. I. Heat of desorption and application of BET theory1. *Journal of the American Chemical Society*, *74*(6), 1367–1371. https://doi.org/10.1021/ja01126a001

Mooney, R. W., Keenan, A. G., & Wood, L. A. (1952b). Adsorption of water vapor by montmorillonite. II. Effect of exchangeable ions and lattice swelling as measured by X-ray diffraction. *Journal of the American Chemical Society*, *74*(6), 1371–1374.

Myers, A. L. (2002). Thermodynamics of adsorption in porous materials. *AIChE Journal*, *48*(1), 145–160. https://doi.org/10.1002/aic.690480115

Newman, A. C. D. (1983). The specific surface of soils determined by water sorption. *Journal of Soil Science*, *34*(1), 23–32. https://doi.org/10.1111/j.1365-2389.1983.tb00809.x

Nishino, J. (2001). Adsorption of water vapor and carbon dioxide at carboxylic functional groups on the surface of coal. *Fuel*, *80*(5), 757–764. https://doi.org/10.1016/S0016-2361(00)00136-8

Quirijns, E. J., van Boxtel, A. J. B., van Loon, W. K. P., & Van Straten, G. (2005). Sorption isotherms, GAB parameters and isosteric heat of sorption. *Journal of the Science of Food and Agriculture*, *85*(11), 1805–1814. https://doi.org/10.1002/jsfa.2140

Salles, F., Beurroies, I., Bildstein, O., Jullien, M., Raynal, J., Denoyel, R., & Van Damme, H. (2008). A calorimetric study of mesoscopic swelling and hydration sequence in solid Na-montmorillonite. *Applied Clay Science*, *39*(3–4), 186–201. https://doi.org/10.1016/j.clay.2007.06.001

Salles, F., Bildstein, O., Douillard, J. M., Jullien, M., Raynal, J., & Van Damme, H. (2010). On the cation dependence of interlamellar and interparticular water and swelling in smectite clays. *Langmuir*, *26*(7), 5028–5037. https://doi.org/10.1021/la1002868

Sang, G., Liu, S., Zhang, R., Elsworth, D., & He, L. (2018). Nanopore characterization of mine roof shales by SANS, nitrogen adsorption, and mercury intrusion: Impact on water adsorption/retention behavior. *International Journal of Coal Geology*, *200*, 173–185. https://doi.org/10.1016/j.coal.2018.11.009

Schuttlefield, J. D., Cox, D., & Grassian, V. H. (2007). An investigation of water uptake on clays minerals using ATR-FTIR spectroscopy coupled with quartz crystal microbalance measurements. *Journal of Geophysical Research*, *112*, D21303. https://doi.org/10.1029/2007JD008973

Seemann, T., Bertier, P., Krooss, B. M., & Stanjek, H. (2017). Water vapour sorption on mudrocks. *Geological Society, London, Special Publications*, *454*(1), 201–233. https://doi.org/10.1144/SP454.8

Sing, K. S. W. (1985). Reporting physisorption data for gas/solid systems with special reference to the determination of surface area and porosity (Recommendations 1984). *Pure and Applied Chemistry*, *57*(4), 603–619. https://doi.org/10.1351/pac198557040603

Sposito, G. (2008). *The chemistry of soils*. London: Oxford University Press.

Švábová, M., Weishauptová, Z., & Přibyl, O. (2011). Water vapour adsorption on coal. *Fuel*, *90*(5), 1892–1899. https://doi.org/10.1016/j.fuel.2011.01.005

Tang, X., Ripepi, N., Valentine, K. A., Keles, C., Long, T., & Gonciaruk, A. (2017). Water vapor sorption on Marcellus shale: Measurement, modeling and thermodynamic analysis. *Fuel*, *209*, 606–614. https://doi.org/10.1016/j.fuel.2017.07.062

Thommes, M., Kaneko, K., Neimark, A. V., Olivier, J. P., Rodriguez-Reinoso, F., Rouquerol, J., & Sing, K. S. W. (2015). Physisorption of gases, with special reference to the evaluation of surface area and pore size distribution (IUPAC Technical Report). *Pure and Applied Chemistry*, *87*(9–10), 1051–1069. https://doi.org/10.1515/pac-2014-1117

Thommes, M., Morell, J., Cychosz, K. A., & Fröba, M. (2013). Combining nitrogen, argon, and water adsorption for advanced characterization of ordered mesoporous carbons (CMKs) and periodic mesoporous organosilicas (PMOs). *Langmuir*, *29*(48), 14,893–14,902. https://doi.org/10.1021/la402832b

Timmermann, E. O. (2003). Multilayer sorption parameters: BET or GAB values? *Colloids and Surfaces A: Physicochemical and Engineering Aspects*, *220*(1–3), 235–260. https://doi.org/10.1016/S0927-7757(03)00059-1

Tuller, M., Or, D., & Dudley, L. M. (1999). Adsorption and capillary condensation in porous media: Liquid retention and interfacial configurations in angular pores. *Water Resources Research*, *35*(7), 1949–1964. https://doi.org/10.1029/1999WR900098

Van Eeckhout, E. M. (1976). *The mechanisms of strength reduction due to moisture in coal mine shales* (Vol. 13, pp. 61–67). Pergamon.

Vidic, R. D., Brantley, S. L., Vandenbossche, J. M., Yoxtheimer, D., & Abad, J. D. (2013). Impact of shale gas development on regional water quality. *Science*, *340*(6134), 1235009. https://doi.org/10.1126/science.1235009

Wan, K., He, Q., Miao, Z., Liu, X., & Huang, S. (2016). Water desorption isotherms and net isosteric heat of desorption on lignite. *Fuel*, *171*, 101–107. https://doi.org/10.1016/j.fuel.2015.12.054

Wang, S., Elsworth, D., & Liu, J. (2011). Permeability evolution in fractured coal: The roles of fracture geometry and water-content. *International Journal of Coal Geology*, *87*(1), 13–25. https://doi.org/10.1016/j.coal.2011.04.009

Woodruff, W. F., & Revil, A. (2011). CEC-normalized clay-water sorption isotherm. *Water Resources Research*, *47*, W11502. https://doi.org/10.1029/2011WR010919

Zhang, S., Sheng, J. J., & Qiu, Z. (2016). Water adsorption on kaolinite and illite after polyamine adsorption. *Journal of Petroleum Science & Engineering*, *142*, 13–20. https://doi.org/10.1016/j.petrol.2016.01.040

Zolfaghari, A., Dehghanpour, H., & Holyk, J. (2017). Water sorption behaviour of gas shales: I. Role of clays. *International Journal of Coal Geology*, *179*, 130–138. https://doi.org/10.1016/j.coal.2017.05.008

Zolfaghari, A., Dehghanpour, H., & Xu, M. (2017). Water sorption behaviour of gas shales: II. Pore size distribution. *International Journal of Coal Geology*, *179*, 187–195. https://doi.org/10.1016/j.coal.2017.05.009